Combined Detection of Surface Changes and Deformation Anomalies Using Amplitude-Augmented Recursive InSAR Time Series

Fengming Hu, *Member, IEEE*, Freek J. van Leijen, *Member, IEEE*, Ling Chang, Jicang Wu, and Ramon F. Hanssen, *Senior Member, IEEE*

***Abstract*— Synthetic aperture radar (SAR) missions with short repeat times enable opportunities for near real-time deformation monitoring. Traditional multitemporal interferometric SAR (MT-InSAR) is able to monitor long-term and periodic deformation with high precision by time-series analysis. However, as time series lengthen, it is time-consuming to update the current results by reprocessing the whole dataset. Additionally, the number of coherent scatterers varies over time due to disappearing and emerging scatterers due to inevitable changes in surface scattering, and potential deformation anomalies require changes in the prevailing deformation model. Here, we propose a novel method to analyze InSAR time series recursively and detect both significant changes in scattering as well as deformation anomalies based on the new acquisitions. Sequential change detection is developed to identify temporary coherent scatterers (TCSs) using amplitude time series. Based on the predicted phase residuals, scatterers with abnormal deformation displacements are identified by a generalized ratio test, while the parameters of stable scatterers are updated using Kalman filtering. The quality of the anomaly detection is assessed based on the detectability power and the minimum detectable deformation. This facilitates (near) real-time data processing and decreases the false alarm likelihood. Experimental results show that the technique can be used for the real-time evaluation of deformation risks.**

***Index Terms*— Anomaly detection, change detection, multitemporal InSAR, recursive process.**

I. Introduction

MULTITEMPORAL interferometric synthetic aperture radar (MT-InSAR) is a powerful tool for measuring deformation of (objects on) the earth with millimeter-level precision. This technique is successfully used in many applications in earth observation including subsidence in urban areas [1], [2], and the monitoring of infrastructure [3], [4], landslides [5], [6], and volcano phenomena [7] since it overcomes limitations due to atmospheric delay [8] as well as spatiotemporal decorrelation noise [9] in differential InSAR.

The first implementation of MT-InSAR is persistent scatterer InSAR [10], [11], which focuses on point-like targets showing high (temporal) coherence throughout the whole time series. Most of these scatterers are related to man-made infrastructure such as buildings and railways [4], [12], [13]. Therefore, its applicability in rural areas is often limited. Compared to point scatterers (PSs), distributed scatterers (DSs) are often found on natural terrain, which is more susceptible to temporal decorrelation. Small BAseline Subset (SBAS) [14], [15] is a typical approach for DS analysis, which only utilizes interferograms with small temporal baselines and applies multilooking to limit the amount of decorrelation.

Other algorithms identify phase-stable scatterers using distinct criteria, such as the maximum likelihood estimation method [16] and local phase analysis [17], which includes PSs and DSs with high coherence. The latest MT-InSAR implementations increase the number of observations by exploiting both PS and DS information. They combine all interferograms to obtain the optimal phase of all DSs. The DS phase optimization is conducted by identifying statistically homogeneous pixels and phase reconstruction by phase triangle analysis (PTA) [18] and extended methods proposed in [19]–[22].

As current synthetic aperture radar (SAR) sensors have lower revisit times and wider swaths, data volumes increase and subsequently the computational burden. Consequently, conventional MT-InSAR algorithms will rapidly reach their limits in terms of processing time. In [23], an efficient processing chain including parallel as well as sequential steps based on P-SBAS is presented for Sentinel-1 stacks. In [24], a recursive estimator based on the Kalman filter is proposed for phase unwrapping with a temporal smoothness constraint. Ansari *et al.* [25] introduced a sequential estimator to achieve an efficient phase-linking approach and get the optimal phase time series of DSs sequentially. In [26], a deformation prediction method is proposed combining time-series InSAR and the

Manuscript received February 10, 2021; revised May 24, 2021 and June 18, 2021; accepted June 24, 2021. This work was supported by the National Nature Science Foundation of China under Grant 42074022. *(Corresponding author: Fengming Hu.)*

This work did not involve human subjects or animals in its research.

Fengming Hu is with the Key Laboratory for Information Science of Electromagnetic Waves (MoE), Fudan University, Shanghai 200433, China (e-mail: fm_hu@fudan.edu.cn).

Freek J. van Leijen and Ramon F. Hanssen are with the Department of Geoscience and Remote Sensing, Delft University of Technology, 2628 Delft, The Netherlands (e-mail: f.j.vanleijen@tudelft.nl; r.f.hanssen@tudelft.nl).

Ling Chang is with ITC, University of Twente, 7500 Enschede, The Netherlands (e-mail: ling.chang@utwente.nl).

Jicang Wu is with the College of Surveying and Geo-Informatics, Tongji University, Shanghai 200092, China (e-mail: jcwu@tongji.edu.cn).

Digital Object Identifier 10.1109/TGRS.2021.3093108

Unscented Kalman Filter (UKF). A recursive process converts the InSAR method to a near real-time monitoring technique with high precision and updates the prevailing deformation model with new observations efficiently. However, updating the phase model using the wrapped phase has a high likelihood of being coincidentally correct, as an arbitrary random sample in the $[-\pi, +\pi)$ range, combined with a significant uncertainty, may end up close to the expected value. This yields a high probability of a false warning.

Deformation time series show different types of temporal patterns, including linear and nonlinear motions, seasonal trends, temperature-related signals, ground motion acceleration, and other potential changes during the acquired period. Apart from the steady-state deformation velocity and spatial gradients, temporal anomalies in the deformation time series are becoming more important since a large deformation within a short time interval may do more harm to the health of infrastructure than gradual long-term deformation [27], [28]. In order to find deformation anomalies within the deformation time series, a post-processing method is proposed in [29], where multiple hypothesis tests are applied to find an optimal kinematic model from a library of canonical functions. This way, both temporal phase unwrapping errors as well as optimal models are detected automatically for all scatterers. Similarly, [30] adopt a multiple linear regression model with m breaks considering $m + 1$ observations to detect an anomalous trend, which is solved by a dynamic programming technique. In [31], different types of anomalies associated with slope instability, subsidence, uplift, and geothermal activity are detected using a continuously updated displacement time series.

However, these post-processing methods only focus on the deformation time series of accepted scatterers in the updated results, while scatterers with significant deformation anomalies may have been discarded during the processing of the whole time series. A feasible approach for detecting a deformation anomaly is to test whether the new observation fits the prevailing deformation model during the interferometric process. For example, in [32], the structural health of a bridge is evaluated by comparing a new observation with prediction intervals, which are determined by the established displacement model and a t-test.

During the interferometric processing, a temporal phase anomaly can be caused by 1) a large deformation or 2) noise in the data. The former should be related to a change in the deformation model, while the latter is caused by phase decorrelation. Unfortunately, we cannot discriminate between these two types of phase anomalies using the interferometric phase since the phase is wrapped, leading to a high probability of false alarms. Pixels exhibiting coherent behavior only over parts of the time series are called temporary coherent scatterers (TCSs) [33], [34].

The amplitude can be strongly related to the properties of ground targets [35], compared to the interferometric phase, and a potential TCS can be identified by analyzing amplitude time series. Assuming a Rayleigh/Rice distribution with a central F-test [36] or Bayesian inference [37], the moment of the abrupt change over the time series (denoted as step-time) can be identified by amplitude change detection for single pixels.

Here, we propose a recursive multitemporal InSAR approach for deformation anomaly detection by subsequently analyzing amplitude and phase updates over time. The main process contains three parts: 1) establishing the initial deformation model, 2) detecting changes based on amplitude analysis, and 3) detecting deformation anomalies. First, a stack of images is processed using an MT-InSAR method and the deformation model for each coherent scatterer is obtained. The established deformation model is used to detect deformation anomalies in the new observation. Second, the relative radiometric calibration factor of the new amplitude is determined and the F-test based on the Rayleigh distribution is used to conduct a single pixel change detection. Then the predicted phase residual of each coherent scatterer is obtained based on the new phase observation, and the χ^2-test is utilized to test whether there is a significant phase anomaly. Additionally, we also introduce quality metrics for the minimal detectable deformation (anomaly) (MDD) considering a given detectability power [29]. Finally, we apply our method to both simulated and real SAR data. The results of the recursive processing are compared with those of the conventional method.

This article is organized as follows. We briefly introduce the MT-InSAR process in Section II, followed by the recursive processing method, anomaly detection, and quality metrics in Section III. Both simulated and real data results are presented in Section IV, followed by the conclusions in Section V.

II. Initialization MT-InSAR Processing

The MT-InSAR methodology involves amplitude as well as phase analysis in a recursive approach.

A. Amplitude Analysis

Both PS candidate selection as well as change detection use amplitude observations from the original single look complex (SLC) images. The original precalibrated SLC amplitude, denoted as a', is post-calibrated empirically using

$$a = \alpha_a a' \tag{1}$$

where a denotes the empirically calibrated amplitude and α_a denotes the radiometric calibration factor. To simplify the process, a relative radiometric calibration is implemented in MT-InSAR [28]. The relative calibration factors refer to the reference (master) image and are calculated for all slave images using stable scatterers selected via the normalized amplitude dispersion (NAD) with a low threshold [10], [28], [38].

With m calibrated amplitude observations a_i for a single pixel, where $i \in [1, m]$ is the acquisition index change detection is conducted by testing whether two contiguous temporal subsets stem from the same Rayleigh distribution. Note that the amplitude values in all the following equations are linear and not in dB. If a significant step is identified between the p^{th} and the $(p+1)^{\text{th}}$ acquisition, the time series is divided into two subsets: $a_1, \ldots, a_p$ and $a_{p+1}, \ldots, a_m$. To test the null hypothesis H_0 that $\sigma_1^2 = \sigma_2^2$, the test statistic

is defined as [39]

$$F_p = \frac{\sum_{i=1}^{p} a_i^2}{2p} \Big/ \frac{\sum_{i=p+1}^{m} a_i^2}{2(m-p)} = \frac{\hat{\sigma}_1^2}{\hat{\sigma}_2^2} \sim F_{2p,2(m-p),0} \quad (2)$$

with a central F-distribution with $2p$ and $2m-2p$ degrees of freedom, where $\hat{\sigma}_1^2$ and $\hat{\sigma}_2^2$ denote the estimated Rayleigh scale parameters of the two subsets [39]. Given a level of significance α, the critical value K_α is obtained. If $\hat{\sigma_1} < \hat{\sigma_2}$, we invert the ratio and the degrees of freedom [39]. This way, we ensure that the F-value is always larger than 1. If $F_p < K_\alpha$, there is no significant difference between the two subsets. Otherwise, the null hypothesis H_0 is rejected, which means a step is detected between image acquisitions p and $p+1$. Consecutively, testing for steps after each acquisition, we obtain the corresponding F-values and find the most significant step located at the maximum of the F-values. Thus, the sequential number of the image preceding the step is

$$\hat{p} = \underset{p=1:m-1}{\operatorname{argmax}} \big(F_p | F_p > K_\alpha\big). \quad (3)$$

If there is more than one significant step within a time series, an iterative binary segmentation approach is adopted. In each iteration, we apply the F-test to identify the step time and split the time series into two subsets. This process is repeated until no further steps exist in the subsets, or until the subsets are shorter than a given threshold. Note that scatterers with identified steps are potential TCS, which implies a significant surface change during the acquisition period.

B. Interferometric Phase Analysis

In MT-InSAR, the basic observations are the differential interferometric phases between pairs of scatterers, denoted as arcs. We estimate the arc's residual height and deformation velocity using time-series analysis. Considering $m-1$ differential single master interferograms from m SAR images, the phase difference between two scatterers i and j of a single arc in the k^{th} interferogram can be expressed as [28], [40]

$$\Delta\phi_{i,j}^k = c_{i,j} - \frac{4\pi}{\lambda}\frac{B_{\perp,i}^k}{R_i \sin\theta_i}\Delta h_{i,j} - \frac{4\pi}{\lambda} B_t^k \Delta v_{i,j} + 2\pi n_{i,j}^k + e_{i,j}^k \quad (4)$$

where $\Delta h_{i,j}$ and $\Delta v_{i,j}$ denote the residual height difference and the velocity difference between the two scatterers, $n_{i,j}^k \in \mathbb{Z}$ denotes the integer phase ambiguity numbers, and B_t^k and $B_{\perp,i}^k$ denote the temporal and perpendicular baseline, respectively. R_i is the slant range, θ_i is the local incidence angle, λ is the radar wavelength, $c_{i,j}$ denotes the phase constant that corresponds to the atmospheric delay difference in the master image, and $e_{i,j}^k$ denotes the random error of the phase, including the atmospheric delay difference in the slave image. Note that we only consider the linear velocity in this initial deformation model—other parameters such as temperature-related parameters may be added to (4). The integer least-squares model of continuously coherent scatterers (CCS, see [36] for the taxonomy) is defined as follows [40]:

$$E\left\{\begin{bmatrix}\Delta\phi_{i,j}^1\\ \vdots \\ \Delta\phi_{i,j}^{m-1}\end{bmatrix}\right\} = \begin{bmatrix}2\pi & 0 & 0\\ 0 & \ddots & 0\\ 0 & 0 & 2\pi\end{bmatrix}\begin{bmatrix}n_{i,j}^1\\ \vdots \\ n_{i,j}^{m-1}\end{bmatrix} - \frac{4\pi}{\lambda}\begin{bmatrix}\frac{B_{\perp,i}^1}{R_i\sin\theta_i} & t^1 & \frac{\lambda}{4\pi}\\ \vdots & \vdots & \vdots \\ \frac{B_{\perp,i}^{m-1}}{R_i\sin\theta_i} & t^{m-1} & \frac{\lambda}{4\pi}\end{bmatrix}\begin{bmatrix}\Delta h_{i,j}\\ \Delta v_{i,j}\\ c_{i,j}\end{bmatrix} \quad (5)$$

where $E\{\cdot\}$ denotes the expectation operator. In the arc solution, the variance–covariance (VC) matrix of the phase observations is determined by variance component estimation (VCE) [34], [41], [42]. Based on the VC-matrix, phase unwrapping is implemented using the Least-squares AMBiguity Decorrelation Adjustment (LAMBDA) method for all arcs [40], [43], and the validation of the ambiguity resolution is tested by the so-called ratio test [44]. Thus, the parameters as well as their precision can be estimated using a least-squares approach and checked by the temporal coherence [11], [45].

The selected CCS candidates, which are obtained via thresholding the NAD, will have different noise levels. Therefore, an agile process is conducted in which scatterers with different qualities are processed with different strategies [28]. A first-order network is constructed using scatterers selected with a low NAD threshold to guarantee high precision of the final result. A Delaunay network is used to establish an initial network and arc solutions are obtained using (5). After removing arcs with low temporal coherence, every isolated scatterer is connected to its neighbors to generate new arcs [45]. Only scatterers that reach a minimal number of connections, for example, 3, are accepted in the reference network. Subsequently, by increasing the NAD threshold, scatterers with a medium noise level are identified, and a second-order network is constructed to link these new scatterers to the first-order network. New arcs are generated by linking every scatterer to its nearest neighbors in the first-order network and these arcs are computed in the same way. Details are shown in [36].

C. Initialization

Several parameters obtained in the initial MT-InSAR processing are saved and used as input for the recursive process.

1) NAD Values: The first elements in the initialization are the NAD values including the average amplitude and amplitude standard deviation for all scatterers. These are used to select the coherent scatterers during the relative calibration.

2) Length of Valid Time Series: The potential step times for all scatterers is obtained during the amplitude analysis with a given level of significance. For recursive processing, only time series from the last step time to the last observation are considered, termed the "valid" time series. The length of each time series for every scatterer is recorded. Note that the scatterers used in the initialization are always CCS and thus the length of a valid time series is equal to the total number of acquisitions.

3) Rayleigh Scale Parameters: The test statistic of the F-test defined in (2) is the ratio of the two estimated Rayleigh scale parameters of the two subsets. Here, the estimated Rayleigh scale parameter of the amplitudes within the valid time series is defined as [39]

$$\hat{\sigma}^2_{\text{Rayleigh},m} = \frac{\sum_{i=p+1}^{m} a_i^2}{2(m-p)} \tag{6}$$

where p is the sequential number of the image preceding the step within the m amplitude observations. For CCS, $p = 0$. Rayleigh scale parameters for all scatterers are retained.

4) Network: The CCS and the accepted arcs generated by both the reference network and the second-order network are retained separately.

5) Parameters and VC Matrix: The vector of estimated parameters in (4), that is, the residual height, velocity, and phase constant, as well as its corresponding VC matrix, are retained.

III. Recursive InSAR and Anomaly Detection

Similar to the initialization procedure, the recursive approach includes both an amplitude and an interferometric phase component. The flowchart is shown in Fig. 1. The recursive approach follows a number of prediction and update steps. The prediction step is conducted to detect observation anomalies by comparing the model used in the initialization with the new measurement update. If no anomaly exists, the prevailing model will be sustained in the update step. Note that both surface change detection as well as deformation anomaly detection are included in the recursive approach.

A. Sequential Relative Calibration

If the initialization is conducted using m images, the recursive processing updates the prevailing model using the $(m+1)^{\text{th}}$ image. The relative calibration is conducted using all stable scatterers, which are selected by thresholding the NAD in the conventional MT-InSAR process [28]. Radiometric calibration of the SAR data is necessary since both radiometric sensor stability and the processing algorithm for the raw data induce variation in amplitude [28], which may lead to less preselected scatterers and a higher false alarm rate. Then, we use these preselected scatterers to estimate the relative calibration factor for each new image relative to the master image of the initial stack.

Based on the retained average amplitude, $\overline{a}_m$, and amplitude standard deviation, σ_{a_m}, the NAD values for all pixels in the $(m+1)^{\text{th}}$ epoch are updated as follows:

$$\text{NAD}_{m+1|m} = \frac{\sigma_{a_{m+1|m}}}{\overline{a}_{m+1|m}} \tag{7}$$

where $\sigma_{a_{m+1|m}}$ and $\overline{a}_{m+1|m}$ are, respectively, the updates of the standard deviation and average of amplitude in the $(m+1)^{\text{th}}$ epoch, which are computed by

$$\overline{a}_{m+1|m} = \frac{\overline{a}_m \cdot m + a_{m+1}}{m+1}, \text{ and} \tag{8}$$

$$\sigma_{a_{m+1|m}} = \sqrt{\frac{m-1}{m}\sigma^2_{a_m} + \frac{(a_{m+1} - \overline{a}_m)^2}{m+1}} \tag{9}$$

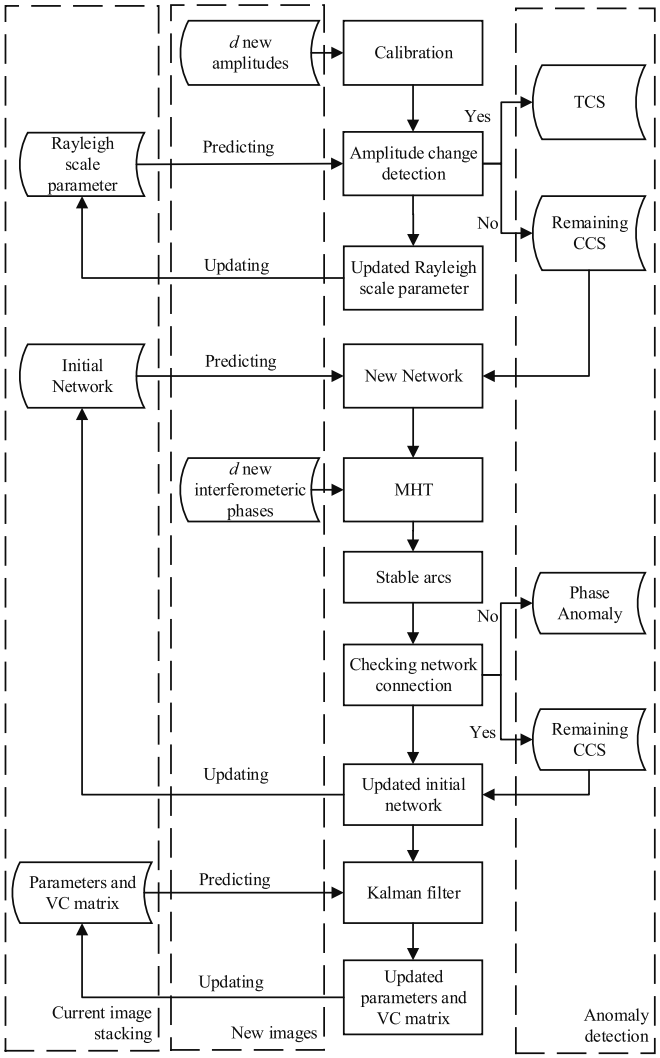

Fig. 1. Flowchart of the recursive InSAR time series and anomaly detection approach.

where a_{m+1} is the $(m+1)^{\text{th}}$ empirically calibrated amplitude. Then stable scatterers are selected with the updated NAD values and the relative radiometric calibration factors of new images are obtained subsequently.

B. Sequential Change Detection

In the prediction step, change detection is implemented using the Rayleigh scale parameter of the initial parameters and the new calibrated amplitude observation. If we add only one new image each time, the F-test becomes

$$F_p = \hat{\sigma}^2_{\text{Rayleigh},m} \Big/ \frac{a^2_{m+1}}{2} \sim F_{2m,2,0}. \tag{10}$$

However, an estimated Rayleigh scale parameter from only one observation is not reliable. Reliability will improve by allowing some more datasets to be acquired, that is, at the expense of timeliness. To test whether a step is located between the m^{th} and the $(m+1)^{\text{th}}$ image using d observations, $a_{m+1}, \ldots, a_{m+d}$ each time, the F-test is defined as

$$F_p = \hat{\sigma}^2_{\text{Rayleigh},m} \Big/ \frac{\sum_{i=m+1}^{m+d} a_i^2}{2d} \sim F_{2m,2d,0}. \tag{11}$$

Postulating a level of significance α, the critical value K_α is obtained. If $F_p < K_\alpha$, there is no surface change in the $(m+1)^{\text{th}}$ image. It is worth noting that most real significant changes, for example, a demolished building, come with a significant amplitude change, and therefore the method will still work even if one of the two subsets contains only very few images. Then, in the update step, the initial Rayleigh scale parameter is updated as

$$\hat{\sigma}^2_{\text{Rayleigh},m+1} = \frac{\hat{\sigma}^2_{\text{Rayleigh},m} \cdot 2m + a^2_{m+1}}{2(m+1)}. \tag{12}$$

If $F_p > K_\alpha$, a step is detected between the m^{th} image and the $(m+1)^{\text{th}}$ image and the updated Rayleigh scale parameter is $a^2_{m+1}/2$.

The problem is that, as time-series lengthen, the NAD parameter is less effective in identifying surface changes in amplitude. The more images the time series will contain, the smaller the effect of one new image will be on the total value. This may lead to a bias in the relative calibration of the new image, which will affect the detectability power of the method. Therefore, amplitude change detection is required to remove the unstable scatterers in an iterative way, to obtain a set of preselected scatterers with sufficient quality.

As the change detection method finds scatterers with a significant change in the new image, a subset of the initial set of CCS will be reclassified as TCS. Subsequently, arcs that contain TCS in the initial network are removed.

C. Ratio Test for Internal Reliability

After change detection using the amplitude observations, the new interferometric phase can be evaluated against the prevailing deformation model. Generally, this process is conducted using a ratio test for internal reliability [44]. Considering the unwrapped phase difference between two scatterers i and j in (5), a model for estimating a static parameter is given by

$$E\left\{\begin{bmatrix}\Delta\phi^1_{i,j}\\ \Delta\phi^2_{i,j}\\ \vdots\\ \Delta\phi^{m-1}_{i,j}\end{bmatrix}\right\} = \begin{bmatrix}A_1\\ A_2\\ \vdots\\ A_{m-1}\end{bmatrix} x_{m-1}, \quad \text{and} \tag{13}$$

$$D\left\{\begin{bmatrix}\Delta\phi^1_{i,j}\\ \Delta\phi^2_{i,j}\\ \vdots\\ \Delta\phi^{m-1}_{i,j}\end{bmatrix}\right\} = \begin{bmatrix}\sigma^2_{\Delta\phi^1_{i,j}} & & & \text{sym}\\ \sigma_{\Delta\phi^{2,1}_{i,j}} & \sigma^2_{\Delta\phi^2_{i,j}} & & \\ \vdots & \vdots & \ddots & \\ \sigma_{\Delta\phi^{m-1,1}_{i,j}} & \sigma_{\Delta\phi^{m-1,2}_{i,j}} & \dots & \sigma^2_{\Delta\phi^{m-1}_{i,j}}\end{bmatrix} \tag{14}$$

where $\sigma^2_{\Delta\phi^k_{i,j}}$ denotes the k^{th} corresponding variance and $\sigma_{\Delta\phi^{k,l}_{i,j}}$ denotes the covariance between the k^{th} and l^{th} interferograms. A_k is design matrix that transforms the parameters into the double difference phases. Parameter vector x_{m-1} contains velocity differences, height residual differences, and phase constants of the arc i–j, estimated at epoch $m-1$. Note that only $m-1$ independent interferometric phase values are possible with m SAR observations. Moreover, note that the proposed recursive process is specifically designed for CCS, which does not consider the decorrelation noise. The VC matrix defined in (14) only describes the system noise in different acquisitions. Thus, one VC matrix is assumed applicable for all arcs. Then the prediction step tests whether the new observation $\Delta\phi^m_{i,j}$ at epoch m fits the phase model built by the initial observations.

Assuming that the new observation fits the prevailing model, the corresponding predicted observation is

$$\Delta\hat{\phi}^{m|m-1}_{i,j} = A_m x_{(m-1)}. \tag{15}$$

An important element in the model test is the predicted residual $\hat{e}_{m|m-1}$. It is the difference between the actual observation and the predicted observation, which is defined as

$$\hat{e}_{m|m-1} = \text{wrap}\left\{\Delta\hat{\phi}^{m|m-1}_{i,j} - \Delta\phi^m_{i,j}\right\} \tag{16}$$

where wrap$\{\cdot\}$ denotes the phase wrapping operator [9]. Here, we assume that a potential change in line-of-sight displacement will be smaller than $\lambda/4$, as the wrapping of a larger displacement will effectively reduce the predicted residual again. The predicted residual of the new observation $\Delta\phi^m_{i,j}$ is here assumed to have statistical properties [46]

$$\hat{e}_{m|m-1} \sim N\left(0, Q_{\hat{e}_{m|m-1}}\right) \tag{17}$$

with corresponding VC matrix

$$Q_{\hat{e}_{m|m-1}} = D\left\{\Delta\phi^m_{i,j}\right\} + A_m D\left\{\hat{x}_{(m-1)}\right\} {A_m}^{\text{T}}. \tag{18}$$

During each observation update, the predicted residual and its VC matrix are available.

The mathematical expressions of the null hypothesis H_0 and the alternative hypothesis H_1 are given by

$$H_0: \; E\left\{\underset{m\times 1}{\Delta\phi_{i,j}}\right\} = \underset{m\times n}{A}\,\underset{n\times 1}{x}; \tag{19}$$

$$H_1: \; E\left\{\underset{m\times 1}{\Delta\phi_{i,j}}\right\} = \begin{bmatrix}\underset{m\times n}{A} & \underset{m\times q}{C_\phi}\end{bmatrix} \underset{(n+q)\times 1}{\begin{bmatrix}x\\ \nabla\end{bmatrix}}, \nabla \neq 0 \tag{20}$$

where matrix C_ϕ and an additional vector of unknown parameters ∇ with length q are used to specify the alternative hypothesis.

The test for an alternative hypothesis follows the test statistic T_q [47], which is given by

$$T_q = \hat{e} Q^{-1}_{\Delta\phi_{i,j}} C_\phi \left(C^T_\phi Q^{-1}_{\Delta\phi_{i,j}} Q_{\hat{e}} Q^{-1}_{\Delta\phi_{i,j}} C_\phi\right)^{-1} C^T_\phi Q^{-1}_{\Delta\phi_{i,j}} \hat{e}. \tag{21}$$

This test statistic has the following distribution under H_0 and H_1:

$$H_0: T_q \sim \chi^2(q,0) \quad H_1: T_q \sim \chi^2(q,\nu) \tag{22}$$

where

$$\nu = \nabla^T C^T_\phi Q^{-1}_{\Delta\phi_{i,j}} Q_{\hat{e}} Q^{-1}_{\Delta\phi_{i,j}} C_\phi \nabla. \tag{23}$$

Given a level of significance α, the critical value $\chi^2_\alpha(q,0)$ is computed using the central χ^2-distribution with q degrees of freedom. We reject H_0 if $T_q > \chi^2_\alpha(q,0)$, which means that a deformation anomaly is detected after the m^{th} phase observation.

D. Deformation Anomaly Detection

Double-difference phase values are obtained for all arcs with each new coregistered SLC image and after removal of the reference phase. In the prediction step, a deformation anomaly detection method is implemented using a ratio test (see Section III-C), jointly with the initial parameters, the VC matrix as well as the new phase observation for all arcs.

Here, we also introduce the process with one observation and d observations separately. Adding one new image each time, the χ^2-test is based on the first predicted phase residual, for example, $q = 1$, $m = 1$, and the $m \times q$ matrix C_ϕ is reduced to a 1×1 matrix $C_\phi = 1$. Thus, the test value is simplified to

$$T_1 = \frac{\hat{e}_m^2}{\sigma_{\hat{e}_m}^2} \sim \chi^2(1, 0) \tag{24}$$

which equals the square of the residual of the m^{th} observation divided by its variance.

Theoretically, we can test a single observation for anomaly detection. However, this approach may be unreliable due to the limited number of observations, leading to a high probability of a false alarm.

An alternative approach is to test whether there is a deformation anomaly after the m^{th} phase observation based on a set of d new update observations, $\Delta\phi_{i,j}^m, \ldots, \Delta\phi_{i,j}^{m+d-1}$, to improve the reliability. Different from the case with one observation, there are different types of deformation anomalies if we consider multiple update observations. Therefore, multiple hypothesis testing (MHT) is adopted to test a set of alternative hypothesis H_j [29] with regard to different types of anomalies. The flowchart of the deformation anomaly detection is shown in Fig. 2. For all H_j, the test statistics are compared with the critical statistical value and test statistic T_q^j follows a χ^2-distribution with different dimensions. Assuming that possible deformation anomalies are limited to decorrelation, offset, and velocity change, a set of possible deformation anomalies is listed below.

1) Offset:

$$C_\phi = [0 \ \cdots \ 0 \ 1 \ 1 \ \cdots \ 1]^T. \tag{25}$$

2) Velocity Increment:

$$C_\phi = \begin{bmatrix} 0 \cdots 0 & \Delta t_1 & \Delta t_2 & \cdots & \Delta t_d \end{bmatrix}^T. \tag{26}$$

3) Offset and Velocity Increment:

$$C_\phi = \begin{bmatrix} 0 \cdots 0 & 1 & 1 & \cdots & 1 \\ 0 \cdots 0 & \Delta t_1 & \Delta t_2 & \cdots & \Delta t_d \end{bmatrix}^T. \tag{27}$$

4) Decorrelation:

$$C_\phi = \begin{bmatrix} 0 \cdots 0 \ 1 \ 0 \cdots 0 \\ 0 \cdots 0 \ 0 \ 1 \cdots 0 \\ \vdots \quad \vdots \ \vdots \ \vdots \ \ddots \ \vdots \\ 0 \cdots 0 \ 0 \ 0 \cdots 1 \end{bmatrix}^T. \tag{28}$$

Four alternative hypothesis tests H_j are built using different C_ϕ with dimensions 1, 1, 2, and d, respectively. Since the test statistic T_q^j follows a χ^2-distribution with different dimensions, we divide the test statistic by its critical value $\chi_{\alpha_j}^2$ to normalize it. When the ratio is greater than 1, the null hypothesis H_0 is rejected. Otherwise, the alternative hypothesis H_j is less likely than H_0, indicating that the scatterer is stable. Therefore, the maximal value of the ratios denotes the most probable alternative hypothesis H_B, if

$$T_q^B = \max_j \left\{ T_q^j / \chi_{\alpha_j}^2 (q_j) \right\}. \tag{29}$$

We reject H_0 if $T_q^B > 1$, which means that there is a deformation anomaly after the m^{th} phase observation. Other types of deformation anomalies, such as seasonal and exponential deformation, can be detected using the same approach with the corresponding C_ϕ, as presented in [29].

Since the results of deformation anomaly detection denote arcs with significant deformation anomalies, these arcs are removed from the initial network. Then, the updated main network is identified by the Depth First Search algorithm (DFS) [48]. Scatterers within the main network are CCS while those that are not connected to the main network are deformation anomalies. This way, the scatterers in the initial network are divided into two groups: CCS and scatterers with a deformation anomaly.

Both detected TCS as well as scatterers with an identified deformation anomaly are removed from the initialization. In the case of subsequent changes in scattering at the same location, for example, demolition of a building followed by

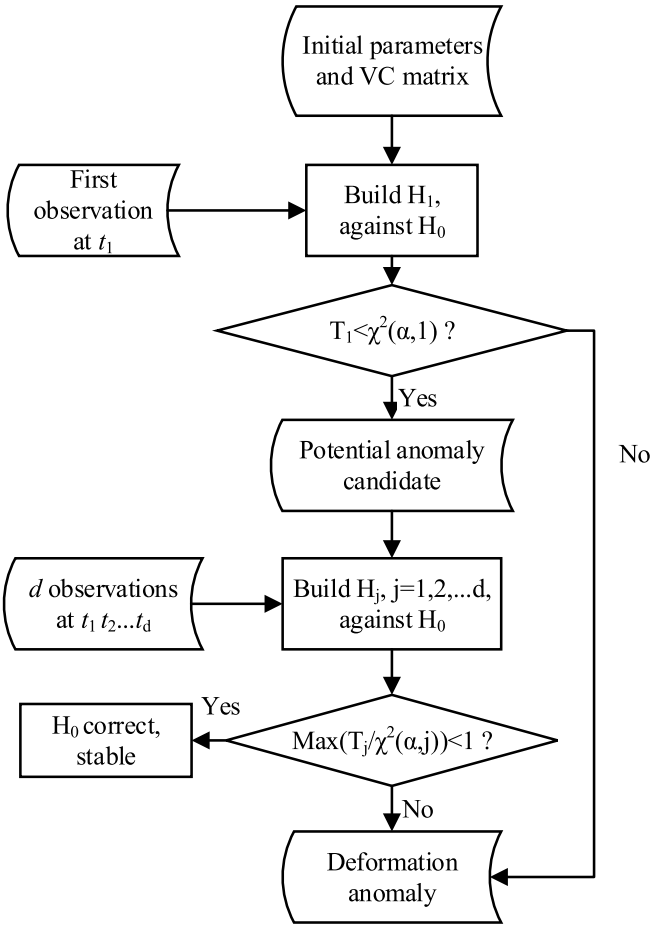

Fig. 2. Deformation anomaly detection using MHT with d observations.

construction of a new building, a minimum number of new acquisitions is required for the temporal phase unwrapping. Thus, the initialization needs to be reprocessed to reestablish a deformation model for the new building. Similarly, considering the detected deformation anomalies, the anomaly detection procedure requires several new updates as well. The reliability of identifying the type of deformation anomalies will be improved by adding more observations.

E. Kalman Filter

In the update step, the initial parameters and corresponding VC matrix for all arcs are updated with a new observation and its variance. First of all, the variance components of the new images are estimated based on the double-difference phase observations of arcs between the CCS in the reference network. Note that independent arcs are selected in the reference network to obtain an unbiased estimation of the variance [40] [28]. Assuming, for now, that the noise of all scatterers is the same within one image, the variance component of double-difference phase between two scatterers at epoch m is defined as

$$\sigma^2_{\Delta\phi^m_{i,j}} = 2DQ_\psi D^T \tag{30}$$

where $Q_\psi = \mathrm{diag}(\sigma^2_{\psi_1}, \sigma^2_{\psi_2})$ is the VC matrix of the two SLC acquisitions, $D = \begin{bmatrix}1 & -1\end{bmatrix}$,and the factor two follows from taking the difference between the two points. Then the variance of the observation at the m^{th} epoch is obtained jointly with the phase residual and the initial VC matrix of the estimated parameters, which is defined as

$$\sigma^2_{\Delta\phi^m_{i,j}} = \hat{e}_m \hat{e}^T_m - A_m Q_{\hat{x}_{(m-1)}} {A_m}^T. \tag{31}$$

The final estimation of the variance component is obtained by averaging the estimated values of the individual arcs. Note that arcs without deformation anomalies are used during the estimation. Thus, the estimation of the variance component is performed iteratively until the estimated phase variances are stabilized. With the estimated variances of the new observations, the update step is implemented using a static Kalman filter. The filtering process is defined as [49]

$$Q_{\hat{x}_{(m)}} = Q_{\hat{x}_{(m-1)}} - GA_m Q_{\hat{x}_{(m-1)}} \tag{32}$$

$$\hat{x}_{(m)} = \hat{x}_{(m-1)} + G\left(\Delta\phi^m_{i,j} - A_m \hat{x}_{(m-1)}\right) \tag{33}$$

where G is the gain matrix, defined as

$$G = Q_{\hat{x}_{(m-1)}} A_m \left(\sigma^2_{\Delta\phi^m_{i,j}} + A_m Q_{\hat{x}_{(m-1)}} {A_m}^T\right)^{-1}. \tag{34}$$

After getting the updated arc solutions, we can estimate parameters of the scatterers by integrating all arc solutions. Note that scatterers in different levels are processed separately without a loss of precision.

F. Quality Metrics of Anomaly Detection

Considering the alternative hypothesis H_1 in (20), the quality metrics for deformation anomaly detection are established using a statistical test. An important value is the MDD [12], which indicates whether a deformation anomaly could be detected with a probability γ_0 based on the VC matrix. This probability is commonly called the detectability power [12].

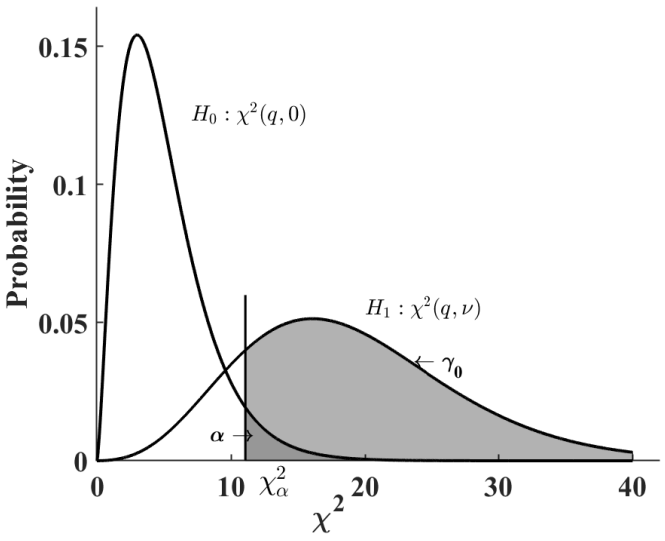

Fig. 3. Probability density functions under the null (no deformation) H_0 and an alternative hypothesis H_1. (q, ν) are the dimension and noncentrality parameter.

Suppose that a γ_0 is fixed, we can calculate the noncentrality parameter ν with a given level of significance α as well as a dimension q [50], which is defined as

$$\nu_0 = \nu\left(\gamma_0, \chi^2_\alpha(q,0), q\right). \tag{35}$$

The relationship between γ_0 and α is shown in Fig. 3. Consequently, the MDD is defined as

$$\nabla_{\text{MDD}} = \frac{\lambda}{4\pi}\sqrt{\frac{\nu_0}{C^T_\phi Q^{-1}_{\Delta\phi_{i,j}} Q_{\hat{e}_{m|m-1}} Q^{-1}_{\Delta\phi_{i,j}} C_\phi}}. \tag{36}$$

On the contrary, with an *a priori* postulated ∇_{MDD}, the noncentrality parameter ν_0 is obtained as

$$\nu_0 = \left(\frac{4\pi}{\lambda}\right)^2 \nabla_{\text{MDD}} C^T_\phi Q^{-1}_{\Delta\phi_{i,j}} Q_{\hat{e}_{m|m-1}} Q^{-1}_{\Delta\phi_{i,j}} C_\phi \nabla_{\text{MDD}} \tag{37}$$

and the detectability power γ_0 is found to be

$$\gamma_0 = F\left(\chi^2_\alpha(q,0)|q,\nu_0\right) \tag{38}$$

where $F(\cdot)$ denotes the cumulative density function (CDF) of the noncentral χ^2 distribution.

In our processing approach, detecting deformation anomalies depends on three parameters, that is, the level of significance α, the detectability power γ_0, and the MDD. Given two of them, the third one can be calculated. This yields two strategies considering the quality metrics, which are listed as follows:

1) Detectability Power γ_0: Given a level of significance and MDD, the detectability power of all scatterers with phase anomalies is calculated. The MDD can be specified based on a certain application. The detection power shows the probability of the detectable deformation anomaly under the given MDD.

2) MDD: Given a level of significance and detectability power, the MDD of all scatterers is obtained. We can obtain the minimal deformation that can be detected based on the specified probability.

IV. Application on Simulated and Real Data

In order to validate the proposed method for deformation anomaly detection and evaluate its performance, we test it on a simulated dataset and demonstrate it on real data from the TerraSAR-X satellite.

A. Deformation Anomaly Detection on Simulated Data

The simulated dataset includes 39 acquisitions, that is, 38 interferograms, and 5000 coherent scatterers over a range of 500 × 500 pixels. Using a radar wavelength of 31.1 mm, a deformation signal $d(x, y, t)$ is simulated by a modified peak function with a maximum deformation velocity of $v_{\max} = 15$ mm/a along the line of sight, that is,

$$d(x, y, t) = t \cdot v_{\max} \cdot \left(\frac{3}{5}(1-x)^2 e^{-x^2-(y+1)^2} - \frac{2}{5}\left(\frac{x}{5} - x^3 - y^5\right) e^{-x^2-y^2} - \frac{1}{5} e^{-(x+1)^2-y^2} \right). \quad (39)$$

The height residual is simulated by assuming a uniform distribution with a maximum value of 10 m. The atmospheric signal is simulated using a power law behavior (see [9]). Additionally, we assume that all scatterers have the same statistics for the phase noise, where we assume a Gaussian distribution with $\sigma = 16°$ for the absolute (unwrapped) phase, which corresponds with a Noise-Equivalent Sigma Zero (NESZ) of −14 dB. After interferogram 35, we add additional displacements to a subset of 200 scatterers, to simulate a change of behavior to be detected with our methodology. Here, an increase in velocity is considered causing additional absolute displacements for interferograms 36, 37, and 38 to increase linearly. These velocities are drawn from a uniform distribution with an absolute range of [1,10] mm per repeat cycle and are referred to as *deformation anomalies* below. All simulated values are then wrapped to the principal 2π interval.

The MT-InSAR method is initialized on the first 35 interferograms, yielding the initial parameters. After the initialization, interferogram 36 is added and the corresponding deformation anomalies are detected using the test metric in (24) with a level of significance of $\alpha = 0.05$. The result is shown in Fig. 4(a), indicating that 172 of the 200 scatterers (86%) with deformation anomalies are successfully detected, while others are not detected. Fig. 5 shows the histograms of the detected and missed (undetected) scatterers, as a function of the deformation anomaly.

Setting a level of significance $\alpha = 0.05$ and a detectability power $\gamma_0 = 0.95$, the MDDs of all scatterers are computed [see (36)]. The average MDD of all scatterers is 2.8 mm. According to the histograms in Fig. 5, most scatterers with deformation anomalies larger than the average MDD are successfully detected, while those with deformation anomalies smaller than the average MDD are not detected. Therefore, the results on simulated data show a good performance of the proposed method.

Considering the quality metrics, both the detectability power and the MDD of all scatterers can be computed, as shown in Fig. 6. The difference of MDD/detectability power between

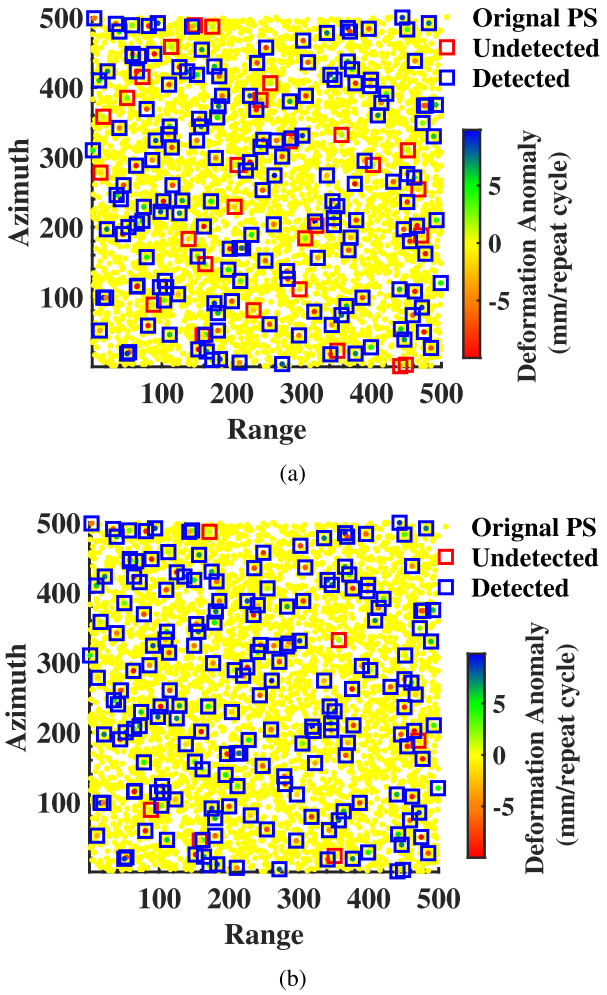

Fig. 4. Deformation anomaly detection by simulated data based on one (a) and three (b) update observations. Blue boxes denote the detected anomalies, while red boxes denote the missed (undetected) anomalies. For one update, 84% of the scatterers with deformation anomalies are successfully detected, while for three updates, this is 97%.

different scatterers is small since the simulated phase noise is the same for all scatterers.

B. Practical Considerations

For practical applications, a user should choose between two approaches. The first approach is to postulate the displacement value to detect, for example, in cases when this displacement value is critical for the failure of a construction. This is termed the *MDD-fixed approach*. With a fixed MDD, we can compute for each point the achievable detectability power. Being overly ambitious in the MDD, that is, requiring a very small MDD, would result in a low detectability power, and hence many missed detections. A more conservative, hence greater, MDD would result in a higher detectability power.

The second approach is to postulate the detectability power, for example, since the consequence of a missed detection may be acceptable or dire. This is termed the *fixed-detectability approach*. Settling with a low detectability results in a low MDD, and hence early detection, albeit with many false detections. Requiring a high detectability results in more correct

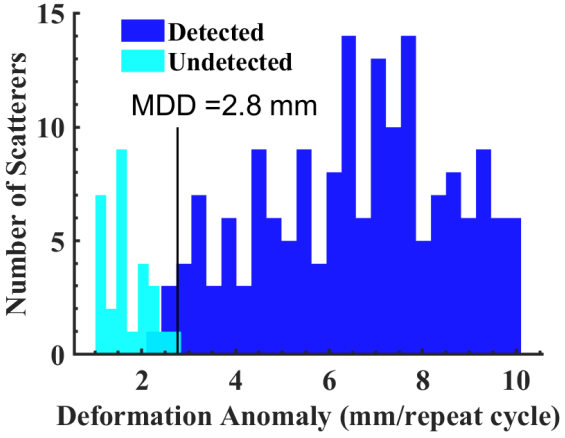

Fig. 5. Histograms of the detected (86%) and missed, or undetected, (14%) scatterers, as a function of the size of the deformation anomaly.

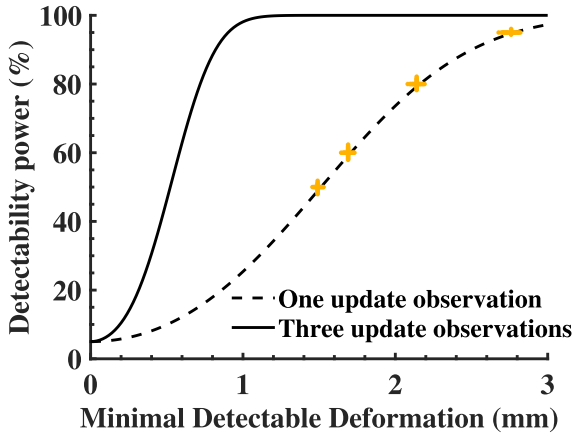

Fig. 6. Relationship between MDD and detectability power for all simulated scatterers. For either an MDD-fixed or a fixed-detectability approach, the corresponding detectability power or MDD can be evaluated, respectively. Yellow dots (aligned as cross-hairs) denote the quality metrics with an MDD-fixed or fixed detectability power approach.

detections, albeit that the displacement needs to be greater to achieve it, hence perhaps a detection at a later time. It is up to the user to decide on the tradeoffs between the incentive to detect even the smallest displacement anomalies, to minimize the adverse impact of not-detecting a critical displacement, and to minimize the number of false warnings.

As described in Section III, the power of detecting a deformation anomaly can also be further improved by adding more update observations, that is, $d > 1$. In this case, we set $d = 3$ and conduct a deformation anomaly detection based on three update observations using MHT described in (29). In the result of the deformation anomaly detection shown in Fig. 4(b), 194 of the 200 scatterers with deformation anomalies are successfully detected (97%). Therefore, by adding update observations, we can improve the capability of the deformation anomaly detection significantly. Additionally, Fig. 6 shows the relationship between MDD and detectability power for one and three update observations, indicating that a larger MDD leads to an increased reliability, or, likewise, that the same MDD can be achieved with a higher detectability power by increasing the number of observations.

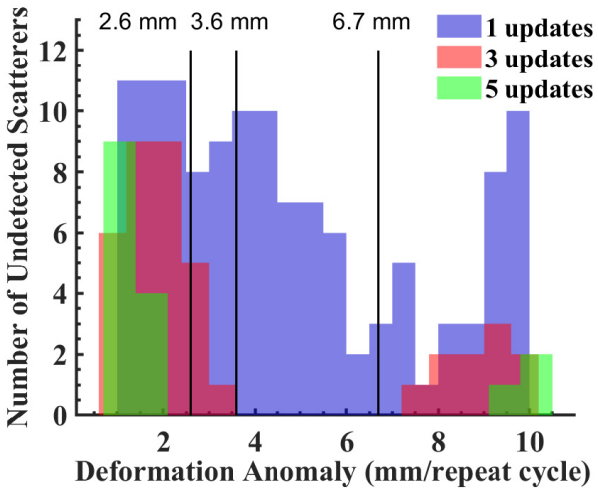

Fig. 7. Histograms of the undetected deformation anomalies with different number of updates. The MDDs with different number of updates are 2.6, 3.6, and 6.7 mm, correspondingly. The percentage of the undetected scatterers are 64% for one update, 20% for three updates, and 10% for five updates.

Because both the detection of a deformation anomaly and the calculation of the two quality metrics depend on the noise-level of the phase, a second simulation is performed using a medium noise level with $\sigma = 35°$, which contains 41 interferograms. The other parameters are the same as in the first simulation. Using a level of significance of $\alpha = 0.05$, the deformation anomaly detection is conducted using one, three, and five updates. Fig. 7 shows that the MDD increases significantly with a higher noise level, leading to more undetected deformation anomalies. Nevertheless, the performance of the deformation anomaly detection can be improved using multiple updates. In this simulation, the percentage of undetected scatterers is 64% for one update, 20% for three updates, and 10% for five updates, indicating that multiple updates help improve the performance of the deformation anomaly detection, especially for data with more noise. However, the reliability of the phase unwrapping in the initialization decreases as the noise level increases, leading to more undetected scatterers with a deformation anomaly larger than the MDD, as shown in Fig. 7. The number of detected scatterers that in fact have no anomaly is 2, 13, and 19, showing an increasing false positive rate with more updates.

The third demonstration is conducted using a composite displacement signal. For the initialization, the displacement signal includes both a linear and a periodic component. Then we add an additional exponential displacement signal, with different scale parameters, to a subset of 200 scatterers. During the deformation anomaly detection, a C_ϕ matrix including offset, linear, and exponential displacement is considered to identify different types of anomalies. Table I represents the number of different types of deformation anomalies with varying number of updates, showing that the various types of deformation anomalies can be obtained accurately with multiple updates.

C. Deformation Anomaly Detection in TerraSAR-X Data

We demonstrate the amplitude-augmented recursive interferometric processing using 60 stripmap TerraSAR-X

TABLE I
DETECTED ANOMALIES GIVEN A DIFFERENT NUMBER OF UPDATES

Number of updates	Offset	Velocity increment	Exponential anomalies	Total
+2	81	64	25	170
+3	50	69	45	164
+5	39	62	63	164

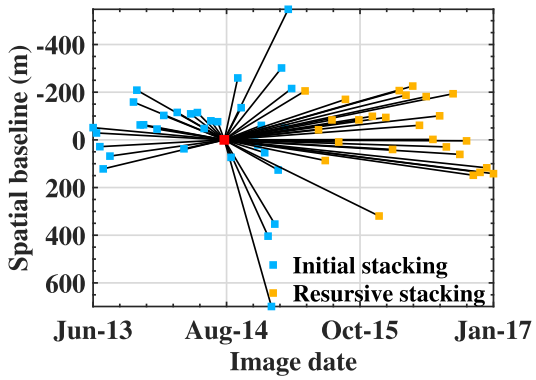

Fig. 8. Distributions of the temporal and spatial baselines. The red dot indicates the master image, blue dots indicate the slave images of the initialization stack, and yellow dots indicate the slave images of the recursive update stack.

images between June 2013 and January 2017 over Delft, The Netherlands. The slant range and azimuth pixel spacings are 1.37 and 1.86 m, respectively. External digital elevation models (DEMs) are not used in our processing and only a flat-earth phase correction is applied during data preprocessing. Fig. 8 shows the distribution of the spatial and temporal baselines. The maximum temporal baseline is less than 900 days and the maximum perpendicular baseline is 600 m. The initialization stack includes the first 34 images, while the recursive stacking includes the other 26 images.

A comparison of the estimated radiometric calibration factors between the conventional and recursive updating approach is shown in Fig. 9(a). Compared with the conventional approach, our recursive approach removes all potential TCS during the calibration, as described in Sections III-A and III-B. The calibration factors on the left side of the dotted line are derived from the initial stack, while the ones on the right side are the recursive updates, showing a significant difference of the calibration factors due to surface changes. To minimize this problem, we introduce an iterative approach in the amplitude processing. First, the relative radiometric calibration is used to obtain initial calibration factors. Then, change detection is implemented based on the empirically calibrated amplitudes, in order to identify scatterers with a significant change, that is, TCS. Subsequently, the relative radiometric calibration is conducted again, but this time only with the selected scatterers that do not change in the time series. The comparison of the estimated radiometric calibration factors between the conventional and the recursive process with change detection is shown in Fig. 9(b), indicating that the bias is corrected by considering the surface changes, which leads to an improved detectability of TCS.

Then CCS in the first-order and second-order network are identified and both the initialization and the whole stack

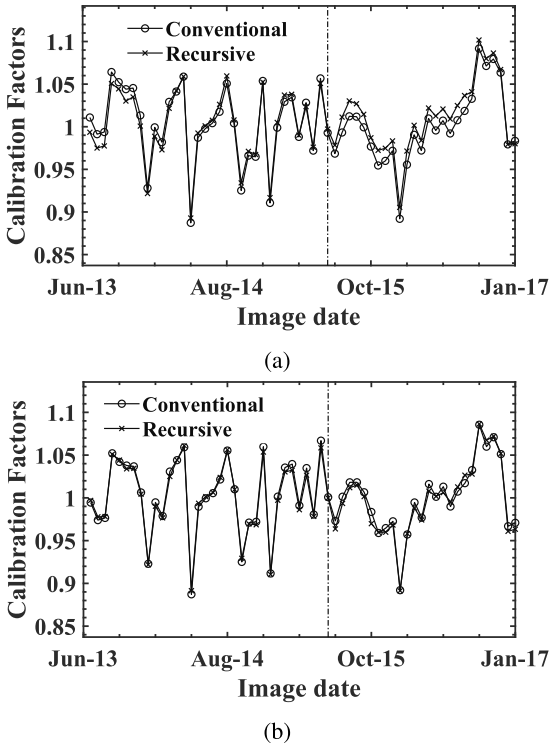

Fig. 9. Estimated radiometric calibration factors by conventional and recursive approach (a) without, and (b) with removal of TCS after change detection.

are processed separately. Fig. 10 shows their corresponding velocity maps with 22 and 18 k scatterers, respectively. The deformation velocity ranges from −13 to 3 mm/a. Comparing Fig. 10(a) and (b), some scatterers located at the southeast of the area disappear if we process a longer time series, which is mainly caused by 1) surface changes or 2) deformation anomalies.

In order to distinguish these two types of anomalies, the proposed recursive update processing is implemented by subsequently analyzing amplitude and interferometric phase. During the recursive process, the sequential change detection on the amplitude is applied where the level of significance in the F-test was set to $\alpha = 0.02$ and identified scatterers with a detected surface change are removed to exclude them from the subsequent phase analysis. Then a χ^2-test is utilized to detect the deformation anomalies with a level of significance of 0.02. Note that the variance of the observations needs to be estimated from the data [see (31)], by evaluating the residues to the prevailing model, and that these estimates have a significant impact on the detectability power of the deformation anomaly. After the deformation anomaly detection, the initial scatterers can be automatically divided into three groups, that is, CCS, TCS, identified by changes in amplitude, and deformation anomalies. Three scatterers in different groups are selected, in Fig. 11, to show both amplitude and deformation time series. Their locations are shown in Fig. 10(a). Based on Fig. 11(a), (c), and (e), the amplitude time series of both the CCS and the deformation anomaly are stable, while that of the TCS shows a significant decrease of amplitude in the 59$^{\text{th}}$ image. Fig. 11(b) indicates that the results by the proposed

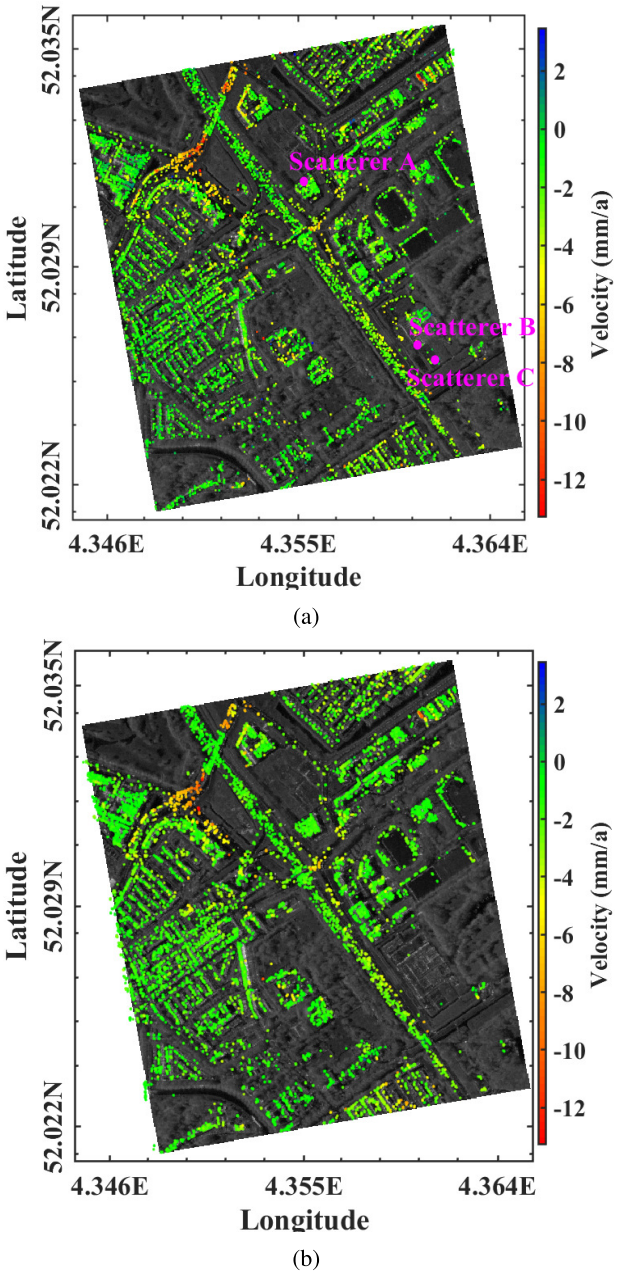

Fig. 10. Velocity on CCS using (a) 34 images (initialization set, with 22 k scatterers) and (b) 60 images (entire set, with 18 k scatterers).

recursive update approach agree well with those of the conventional approach since CCS is stable over the whole time series. Fig.11(d) and (f) shows the deformation time series of the TCS and the deformation anomaly, which would be regarded as CCS in the conventional process. It is obvious that both decorrelation and an inappropriate deformation model will bias the estimated velocity. However, the decorrelation cannot be detected by the phase since the wrapped phase can be coincidentally correct [see the last displacement in Fig. 11(d)]. Compared with the decorrelation, a deformation anomaly leads to a more significant bias of the velocity [see Fig. 11(f)].

All detected deformation anomalies and TCS from the 35th to the 60th images are shown in Fig. 12. Note that the moments of both surface change and deformation anomaly on different

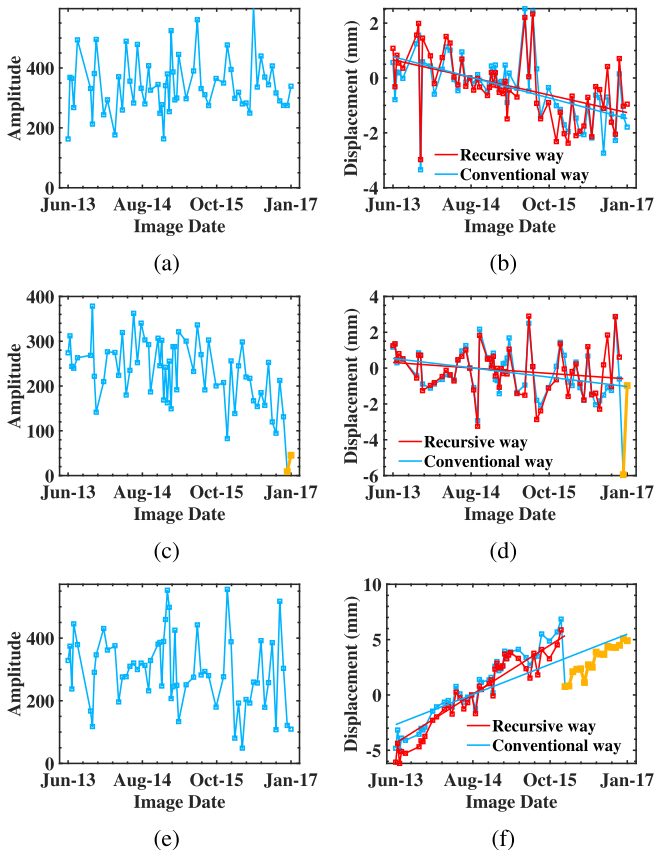

Fig. 11. Comparison of both amplitude and deformation time series on selected scatterers in different groups. First column: amplitude time series. Second column: deformation time series. (a) and (b) CCS. (c) and (d) TCS. (e) and (f) Deformation anomaly. The blue and red lines in (b), (d), and (f) indicate the estimated velocities.

scatterers vary. Two small regions, A and B, are selected to show more details. Region A shows many TCSs, while region B contains some deformation anomalies. Fig. 13(a) shows the amplitude time series of several TCS in selected region A, indicating a decrease of amplitude after the 36th image, which suggests that a destruction occurred between December 2014 and February 2015. Fig. 13(b) shows the deformation time series of five deformation anomalies in the region B. The deformation time series is obtained using the conventional process with the whole 60 images and thus these five scatterers are regarded as CCS. However, there is a significant offset at the 46th epoch, which is a change of deformation model rather than a phase unwrapping error since it is smaller than one-quarter of the radar wavelength.

D. Comparison Between One and Three Updates

A comparison of the detection results with one and three update observations is conducted to demonstrate its impact on the sensitivity of detecting anomalies.

Fig. 14(a) and (b) shows examples of an amplitude time series of a TCS and a deformation time series of a deformation anomaly and their corresponding 98% confidence intervals. The confidence interval of the amplitude is centered at the mean amplitude over the initialization interval, while that of the deformation is centered at the last observation

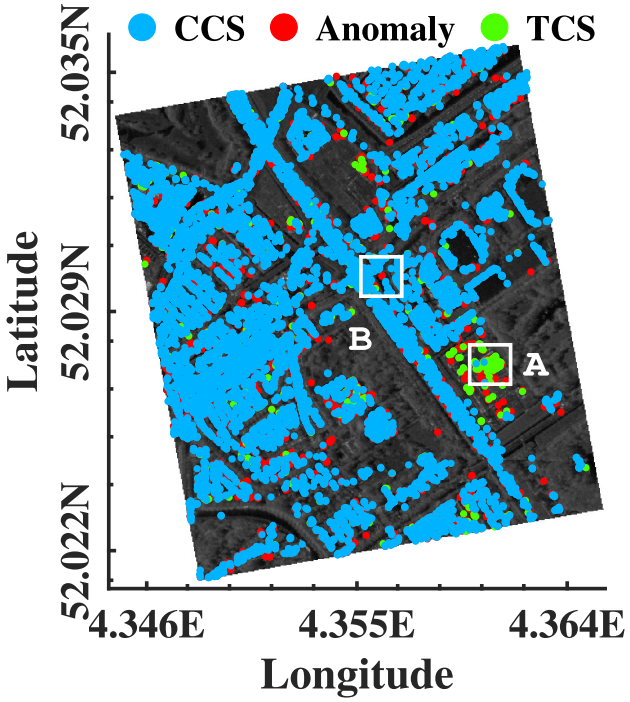

Fig. 12. Result of deformation anomaly detection in the 60th image, with test areas A and B evaluated in Fig. 13.

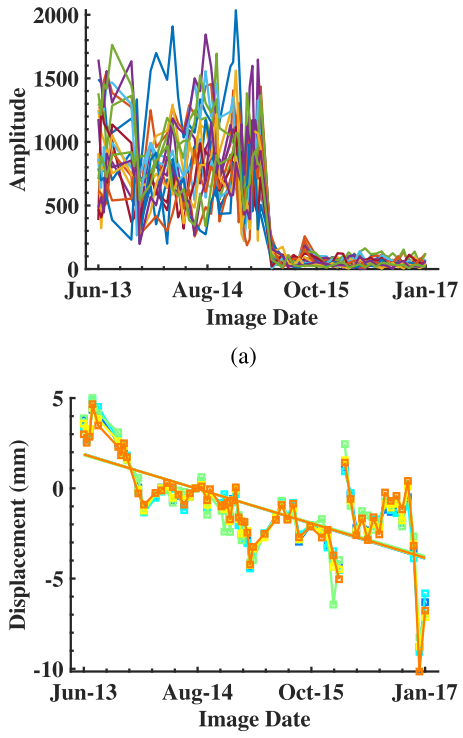

Fig. 13. (a) Amplitude time series of the TCS in region A of Fig 12. (b) Deformation time series of the deformation anomalies in the region B of Fig 12.

in the initialization. In the displacement time series shown in Fig. 14(b), the velocity increases after the offset, leading to a bias of the estimated velocity. However, this increasing velocity cannot be detected by one image update since it does

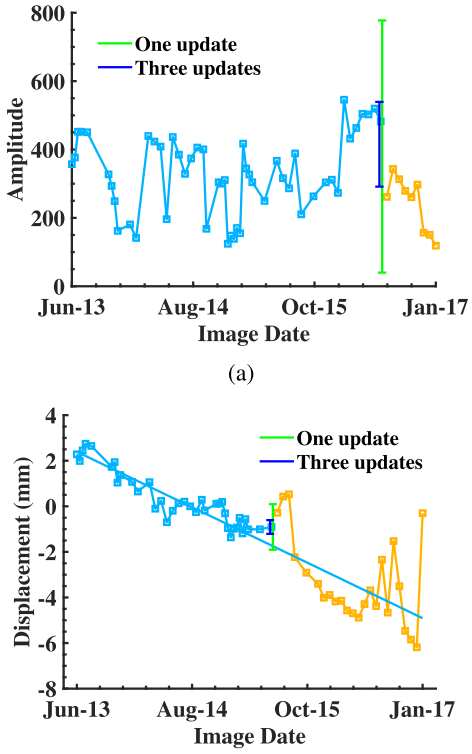

Fig. 14. Confidence interval of amplitude with one and three updates. The blue and green error bars denote a 98% confidence interval.

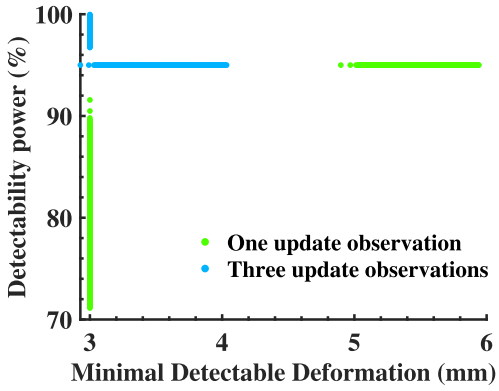

Fig. 15. Quality metrics between one and three update observations with an MDD-fixed or fixed-detectability power approach.

not have an impact on the whole velocity. If the anomaly detection is conducted by three update observations, this type of anomaly can be detected, which demonstrates that we can detect smaller deformation anomalies if we use more update observations.

Then the quality metrics of all scatterers between one and three updates are obtained (see Fig. 15), showing that the MDD obtained by three update observations is smaller than that by the single update observation with the same detectability power. In addition, results by three update observations achieve a higher detectability power than those by one update observation with a given MDD, which means that the detection results by testing three update observations are more reliable/powerful strategy.

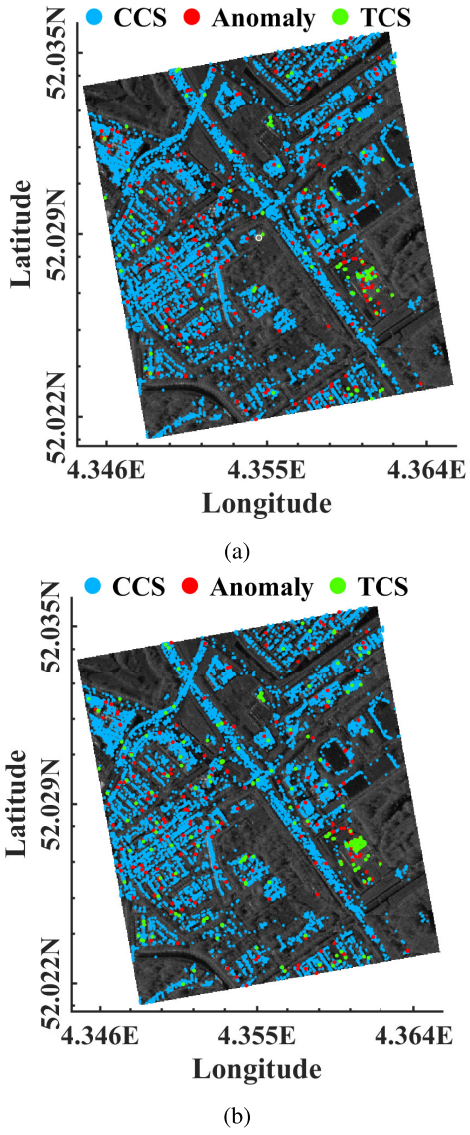

Fig. 16. Comparison of amplitude-augmented anomaly detection between (a) one update observation and (b) three update observations.

Fig. 16 shows the results of anomaly detection in the 40th image using one and three updates. The number of identified TCS in Fig. 16(b) is more than that in Fig. 16(a) since the confidence interval of amplitude with one update is large. Thus, both change detection and deformation anomaly detection with three updates gives a smaller confidence interval, leading to a lower probability of falsely detection.

The following two comparisons demonstrate the importance of incorporating the amplitude in the process. Detection results are obtained by both amplitude-augmented and phase-only anomaly detection, respectively. The first comparison (see Fig. 17), demonstrates the difference of the two results in the spatial domain. Comparing Fig. 17(a) and (b), both detection results identify anomalies that happened on the scatterers within the white box. However, these scatterers are actually surface changes according to Google Earth maps [cf. Fig. 17(c) and (d)], showing that detection results by a phase-only approach have a high false alarm rate, since they cannot separate surface change from deformation anomalies.

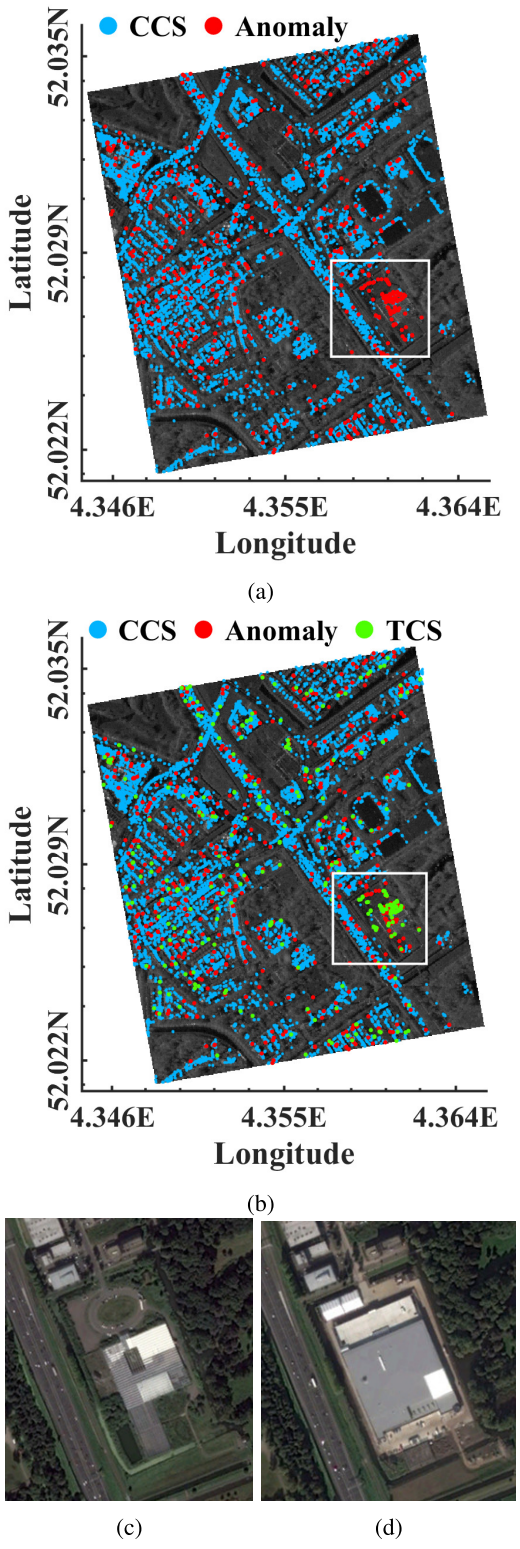

Fig. 17. Comparison between amplitude-augmented anomaly detection and phase-only anomaly detection. (a) Result in 40th image by phase anomaly detection. (b) Result in 40th image by amplitude-augmented anomaly detection. (c) and (d) Google Earth images. White box shows the area with a building change. Note that the 40th image is acquired on September 15, 2015. The acquisition dates of Google Earth images are August 27, 2014, and October 11, 2015, respectively.

The second example shows the sensitivity of the amplitude on the anomalies, which is shown in Fig. 18. Two areas with significant differences in the two detection results are selected,

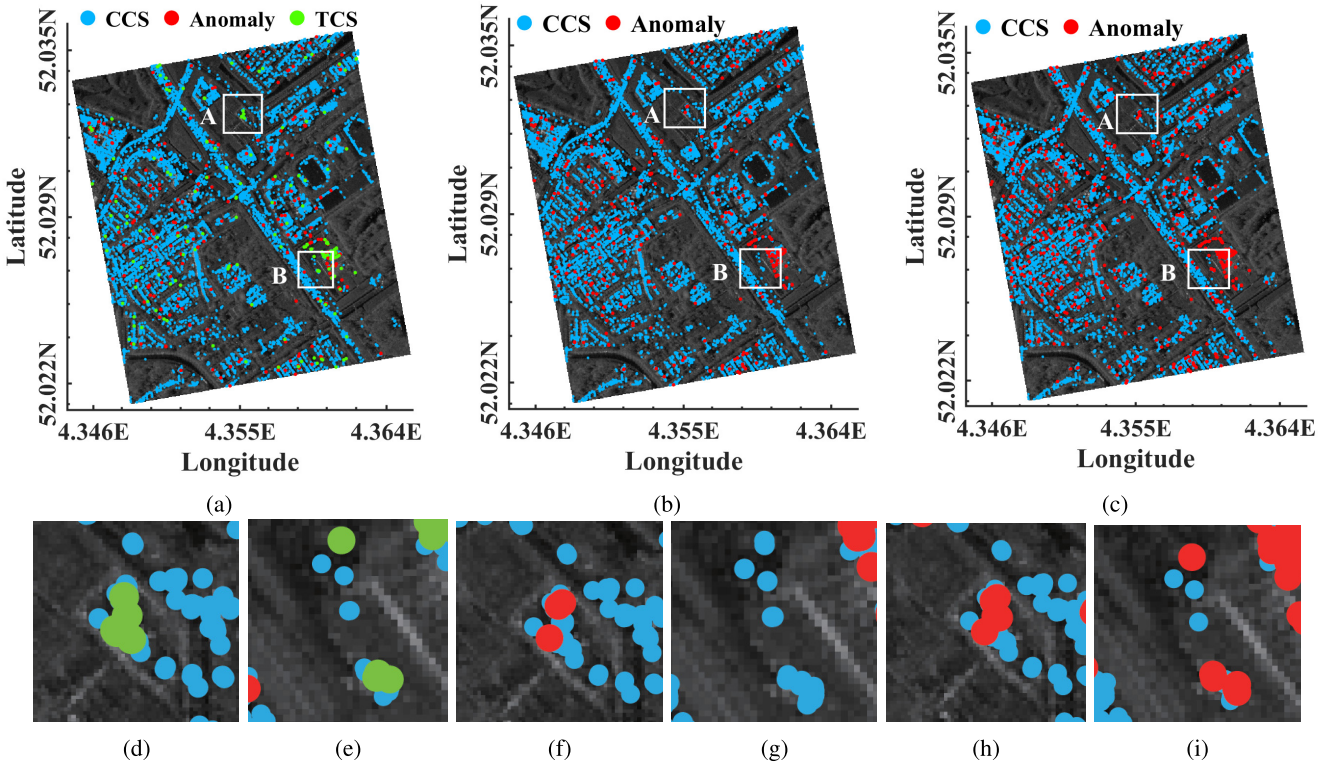

Fig. 18. Comparison between amplitude-augmented anomaly detection and phase anomaly detection. (a) Denotes the result of detection in 38th image by amplitude-augmented anomaly detection. (b) and (c) Results from 39th to 40th images by phase-only anomaly detection. White rectangles show area with significant difference between two approaches. (d)–(i) Magnified views of the selected areas. (d), (f), and (h) Region A. (e), (g), and (i) Region B. (d) and (e) are from (a). (f) and (g) are from (b). (h) and (i) are from (c).

which are marked by the two white rectangles in Fig. 18. From the magnified view in Fig. 18(d) and (e), surface changes in the 38th image over the two selected areas are detected by amplitude change detection. However, detection result by phase-only approach [see Fig. 18(f) and (g)] does not find these anomalies in the 39th image. Furthermore, these surface changes are regarded as deformation anomalies by phase-only approach in the 40th image [see Fig. 18(h) and (i)]. This implies that amplitude is more sensitive to surface change than phase, and results by phase-only anomaly detection do not only have high false alarm rates but also high omission errors.

V. Conclusion

A novel method for deformation anomaly detection is proposed based on an amplitude-augmented recursive InSAR approach. Assuming a Rayleigh distribution, an F-test is used to recursively detect single pixel changes. For the phase, a χ^2-test is used to test the stability per arc-over time, and the initial parameters and VC matrix are updated with new phase observations using a static Kalman filter. We find that amplitude is typically more sensitive to a surface change than phase since the amplitude is associated with the electromagnetic properties of the ground targets, while the phase can be coincidentally correct when the surface changes lead to a phase close to the expected (wrapped) value. Thus, detecting deformation anomalies by combining amplitude and phase observations decreases the number of false alarms.

During the recursive process, anomaly detection is evaluated by adding both one and multiple update observations, where it is shown that the latter can improve the reliability of both a surface change and a deformation anomaly, at the expense of timeliness. Additionally, the detectability power and the MDD are metrics introduced for quality assessment and users can choose an appropriate indicator based on their needs. Tests on simulated and real data show that our recursive process successfully detects deformation anomalies which would be missed in a conventional MT-InSAR process and the proposed amplitude-augmented approach shows a good performance in separating deformation anomalies from surface changes.

The sensitivity of both detecting surface changes and deformation anomalies depends on the choice of the significance level α. Decreasing α will reduce the number of falsely detected TCS in amplitude change detection, as well as the number of false deformation anomalies in ratio test, but will lead to a decreased detectability of true anomalies.

While the proposed recursive framework is designed for PS, an extension is possible for medium-to-low coherent DS. Interferograms would have to be generated using subsequent SAR acquisitions instead of using a single master stack, since DS typically suffer more from temporal decorrelation. Multilooking would be required to improve the coherence estimation, while the change detection should be conducted using a multipixel strategy to improve the reliability due to the speckle noise.

Acknowledgment

The authors acknowledge the German Aerospace Center DLR for the scientific use of TerraSAR-X images.

The attribution of the background maps is to Google Earth Pro, DigitalGlobe 2018 (October 11, 2015 and August 27, 2014), Delft, The Netherlands, 52°N, 4°E [May 2019].

REFERENCES

[1] B. Zhang, R. Wang, Y. Deng, P. Ma, H. Lin, and J. Wang, "Mapping the yellow river delta land subsidence with multitemporal SAR interferometry by exploiting both persistent and distributed scatterers," *ISPRS J. Photogramm. Remote Sens.*, vol. 148, pp. 157–173, Feb. 2019.

[2] L. Zhou *et al.*, "Wuhan surface subsidence analysis in 2015–2016 based on sentinel-1A data by SBAS-InSAR," *Remote Sens.*, vol. 9, no. 10, p. 982, Sep. 2017.

[3] I. E. Özer, S. J. H. Rikkert, F. J. van Leijen, S. N. Jonkman, and R. F. Hanssen, "Sub-seasonal levee deformation observed using satellite radar interferometry to enhance flood protection," *Sci. Rep.*, vol. 9, no. 1, p. 2646, Dec. 2019.

[4] J. Wu and F. Hu, "Monitoring ground subsidence along the Shanghai Maglev zone using TerraSAR-X images," *IEEE Geosci. Remote Sens. Lett.*, vol. 14, no. 1, pp. 117–121, Jan. 2017.

[5] Q. Sun, L. Zhang, X. L. Ding, J. Hu, Z. W. Li, and J. J. Zhu, "Slope deformation prior to Zhouqu, China landslide from InSAR time series analysis," *Remote Sens. Environ.*, vol. 156, pp. 45–57, Jan. 2015.

[6] R. Czikhardt, J. Papco, M. Bakon, P. Liscak, P. Ondrejka, and M. Zlocha, "Ground stability monitoring of undermined and landslide prone areas by means of Sentinel-1 multi-temporal InSAR, case study from Slovakia," *Geosciences*, vol. 7, no. 3, p. 87, Sep. 2017.

[7] A. Hooper, P. Segall, and H. Zebker, "Persistent scatterer interferometric synthetic aperture radar for crustal deformation analysis, with application to Volcán Alcedo, Galápagos," *J. Geophys. Res., Solid Earth*, vol. 112, no. B7, pp. 1–21, 2007.

[8] H. A. Zebker, P. A. Rosen, and S. Hensley, "Atmospheric effects in interferometric synthetic aperture radar surface deformation and topographic maps," *J. Geophys. Res., Solid Earth*, vol. 102, no. B4, pp. 7547–7563, Apr. 1997.

[9] R. F. Hanssen, *Radar Interferometry: Data Interpretation and Error Analysis*. Dordrecht, The Netherlands: Kluwer, 2001.

[10] A. Ferretti, C. Prati, and F. Rocca, "Permanent scatterers in SAR interferometry," *IEEE Trans. Geosci. Remote Sens.*, vol. 39, no. 1, pp. 8–20, Jan. 2001.

[11] A. Ferretti, C. Prati, and F. Rocca, "Nonlinear subsidence rate estimation using permanent scatterers in differential SAR interferometry," *IEEE Trans. Geosci. Remote Sens.*, vol. 38, no. 5, pp. 2202–2212, Sep. 2000.

[12] L. Chang, R. P. B. J. Dollevoet, and R. F. Hanssen, "Monitoring line-infrastructure with multisensor SAR interferometry: Products and performance assessment metrics," *IEEE J. Sel. Topics Appl. Earth Observ. Remote Sens.*, vol. 11, no. 5, pp. 1593–1605, May 2018.

[13] F. Hu, F. J. V. Leijen, L. Chang, J. Wu, and R. F. Hanssen, "Monitoring deformation along railway systems combining multi-temporal InSAR and LiDAR data," *Remote Sens.*, vol. 11, no. 19, p. 2298, Oct. 2019. [Online]. Available: https://www.mdpi.com/2072-4292/11/19/2298

[14] P. Berardino, G. Fornaro, R. Lanari, and E. Sansosti, "A new algorithm for surface deformation monitoring based on small baseline differential SAR interferograms," *IEEE Trans. Geosci. Remote Sens.*, vol. 40, no. 11, pp. 2375–2383, Nov. 2002.

[15] R. Lanari, O. Mora, M. Manunta, J. J. Mallorqui, P. Berardino, and E. Sansosti, "A small-baseline approach for investigating deformations on full-resolution differential SAR interferograms," *IEEE Trans. Geosci. Remote Sens.*, vol. 42, no. 7, pp. 1377–1386, Jul. 2004.

[16] P. Shanker and H. Zebker, "Persistent scatterer selection using maximum likelihood estimation," *Geophys. Res. Lett.*, vol. 34, no. 22, pp. 1–4, 2007.

[17] A. Hooper, "A multi-temporal InSAR method incorporating both persistent scatterer and small baseline approaches," *Geophys. Res. Lett.*, vol. 35, no. 16, 2008, Art. no. L16302.

[18] A. Ferretti, A. Fumagalli, F. Novali, C. Prati, F. Rocca, and A. Rucci, "A new algorithm for processing interferometric data-stacks: SqueeSAR," *IEEE Trans. Geosci. Remote Sens.*, vol. 49, no. 9, pp. 3460–3470, Sep. 2011.

[19] G. Fornaro, S. Verde, D. Reale, and A. Pauciullo, "CAESAR: An approach based on covariance matrix decomposition to improve Multibaseline–Multitemporal interferometric SAR processing," *IEEE Trans. Geosci. Remote Sens.*, vol. 53, no. 4, pp. 2050–2065, Apr. 2015.

[20] S. Samiei-Esfahany, J. E. Martins, F. van Leijen, and R. F. Hanssen, "Phase estimation for distributed scatterers in InSAR stacks using integer least squares estimation," *IEEE Trans. Geosci. Remote Sens.*, vol. 54, no. 10, pp. 5671–5687, Oct. 2016.

[21] S. Navneet, J.-W. Kim, and Z. Lu, "A new InSAR persistent scatterer selection technique using Top eigenvalue of coherence matrix," *IEEE Trans. Geosci. Remote Sens.*, vol. 56, no. 4, pp. 1969–1978, Apr. 2018.

[22] H. Ansari, F. De Zan, and R. Bamler, "Efficient phase estimation for interferogram stacks," *IEEE Trans. Geosci. Remote Sens.*, vol. 56, no. 7, pp. 4109–4125, Jul. 2018.

[23] M. Manunta *et al.*, "The parallel SBAS approach for Sentinel-1 interferometric wide swath deformation time-series generation: Algorithm description and products quality assessment," *IEEE Trans. Geosci. Remote Sens.*, vol. 57, no. 9, pp. 6259–6281, Sep. 2019.

[24] Q. Verburg, "QUInSAR: Temporal parameter and ambiguity estimation using recursive least-squares: A methodology for persistent scatterer interferometry," M.S. thesis, Dept. Geosci. Remote Sens., Delft Univ. Technol., Delft, The Netherlands, 2017.

[25] H. Ansari, F. De Zan, and R. Bamler, "Sequential estimator: Toward efficient InSAR time series analysis," *IEEE Trans. Geosci. Remote Sens.*, vol. 55, no. 10, pp. 5637–5652, Oct. 2017.

[26] F. Xue and X. Lv, "Applying time series interferometric synthetic aperture radar and the unscented Kalman filter to predict deformations in Maoxian landslide," *J. Appl. Remote Sens.*, vol. 13, no. 1, 2019, Art. no. 014509.

[27] F. J. van Leijen and R. F. Hanssen, "Persistent scatterer interferometry using adaptive deformation models," in *Proc. ESA ENVISAT Symp.*, Montreux, Switzerland, Apr. 2007, pp. 23–27. [Online]. Available: http://doris.tudelft.nl/Literature/

[28] F. J. van Leijen, "Persistent scatterer interferometry based on geodetic estimation theory," Ph.D. dissertation, Dept. Geosci. Remote Sens., Delft Univ. Technol., Delft, The Netherlands, 2014.

[29] L. Chang and R. F. Hanssen, "A probabilistic approach for InSAR time-series postprocessing," *IEEE Trans. Geosci. Remote Sens.*, vol. 54, no. 1, pp. 421–430, Jan. 2016.

[30] M. Zhu *et al.*, "Detection of building and infrastructure instabilities by automatic spatiotemporal analysis of satellite SAR interferometry measurements," *Remote Sens.*, vol. 10, no. 11, p. 1816, Nov. 2018.

[31] F. Raspini *et al.*, "Continuous, semi-automatic monitoring of ground deformation using Sentinel-1 satellites," *Sci. Rep.*, vol. 8, no. 1, pp. 1–11, Dec. 2018.

[32] Q. Huang, M. Crosetto, O. Monserrat, and B. Crippa, "Displacement monitoring and modelling of a high-speed railway bridge using C-band Sentinel-1 data," *ISPRS J. Photogramm. Remote Sens.*, vol. 128, pp. 204–211, Jun. 2017.

[33] A. Ferretti, C. Colesanti, D. Perissin, C. Prati, and F. Rocca, "Evaluating the effect of the observation time on the distribution of SAR permanent scatterers," in *Proc. 3rd Int. Workshop ERS SAR Interferometry (FRINGE)*, Frascati, Italy, Dec. 2003, pp. 1–5.

[34] L. Zhang, "Temporarily coherent point SAR interferometry," Ph.D. dissertation, Dept. Land Surveying Geo-Inform., Hong Kong Polytech. Univ., Hong Kong, 2012.

[35] D. Perissin and A. Ferretti, "Urban-target recognition by means of repeated spaceborne SAR images," *IEEE Trans. Geosci. Remote Sens.*, vol. 45, no. 12, pp. 4043–4058, Dec. 2007.

[36] F. Hu, J. Wu, L. Chang, and R. F. Hanssen, "Incorporating temporary coherent scatterers in multi-temporal InSAR using adaptive temporal subsets," *IEEE Trans. Geosci. Remote Sens.*, vol. 57, no. 10, pp. 7658–7670, Oct. 2019.

[37] H. Ansari, N. Adam, and R. Brcic, "Amplitude time series analysis in detection of persistent and temporal coherent scatterers," in *Proc. IEEE Geosci. Remote Sens. Symp.*, Jul. 2014, pp. 2213–2216.

[38] V. B. H. Ketelaar, "Monitoring surface deformation induced by hydrocarbon production using satellite radar interferometry," Ph.D. dissertation, Delft Inst. Earth Observ. Space Syst., Delft Univ. Technol., Delft, The Netherlands, Sep. 2008.

[39] M. M. Siddiqui, "Some problems connected with Rayleigh distributions," *J. Res. Nat. Bureau Standards*, vol. 66, no. 2, pp. 167–174, 1962.

[40] B. M. Kampes and R. F. Hanssen, "Ambiguity resolution for permanent scatterer interferometry," *IEEE Trans. Geosci. Remote Sens.*, vol. 42, no. 11, pp. 2446–2453, Nov. 2004. [Online]. Available: http://doris.tudelft.nl/Literature/kampes04.pdf

[41] B. M. Kampes, *Radar Interferometry*. Dordrecht, The Netherlands: Springer, 2006.

[42] P. J. G. Teunissen and A. R. Amiri-Simkooei, "Least-squares variance component estimation," *J. Geodesy*, vol. 82, no. 2, pp. 65–82, Feb. 2008.

[43] P. J. G. Teunissen, P. J. de Jonge, and C. C. J. M. Tiberius, "The LAMBDA-method for fast GPS processing," in *Proc. GPS Technol. Appl.*, Bucharest, Romania, Sep. 1995, pp. 26–29.
[44] S. Verhagen and P. J. G. Teunissen, "New global navigation satellite system ambiguity resolution method compared to existing approaches," *J. Guid., Control, Dyn.*, vol. 29, no. 4, pp. 981–991, Jul. 2006.
[45] F. Hu and J. Wu, "Improvement of the multi-temporal InSAR method using reliable arc solutions," *Int. J. Remote Sens.*, vol. 39, no. 10, pp. 3363–3385, May 2018.
[46] P. Teunissen and M. Salzmann, "A recursive slippage test for use in state-space filtering," *Manuscripta Geodaetica*, vol. 14, pp. 383–390, Oct. 1989.
[47] P. J. Teunissen, "Adjusting and testing with the models of the affine and similarity," *Manuscripta Geodaetica*, vol. 11, pp. 214–225, May 1986.
[48] S. Even, *Graph Algorithms*. Cambridge, U.K.: Cambridge Univ. Press, 2011.
[49] R. E. Kalman, "A new approach to linear filtering and prediction problems," *J. Basic Eng.*, vol. 82, no. 1, pp. 35–45, Mar. 1960.
[50] W. Baarda, *A Testing Procedure for use in Geodetic Networks* (Publications on Geodesy), 2nd ed, vol. 5. Delft, The Netherlands: Netherlands Geodetic Commission, 1968.

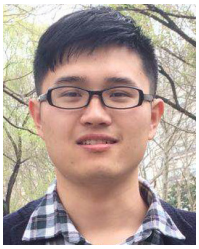

Fengming Hu (Member, IEEE) received the B.E. and Ph.D. degrees from Tongji University, Shanghai, China, in 2014 and 2020, respectively.

During the period October 2017–October 2019, he was a Guest Ph.D. Student with the Delft University of Technology, Delft, the Netherlands. Since 2020, he has been a Post-Doc with the Key Laboratory for Information Science of Electromagnetic Waves (MoE), Fudan University, Shanghai. His interest includes deformation monitoring, 3-D model of the infrastructures, urban change detection, and dynamic data processing using synthetic aperture radar images.

Freek J. van Leijen (Member, IEEE) received the master's degree in geodetic engineering from the Delft University of Technology, Delft, The Netherlands, in 2002.

His thesis concerned the stochastic modeling of the tropospheric variability using global positioning system (GPS) and InSAR observations. In 2003, he rejoined the Delft University of Technology as a Ph.D. student, working on InSAR Research. He has developed a range of software algorithms for persistent scatterer interferometry. After working five years at SkyGeo, a commercial company delivering radar remote sensing services, he returned to the Delft University of Technology in 2013 to continue his research in the field of satellite radar interferometry.

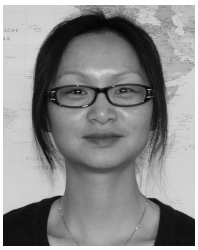

Ling Chang received the M.S.E. degree in geodesy and survey engineering from Tongji University, Shanghai, China, in 2010, and the Ph.D. degree from the Delft University of Technology, Delft, The Netherlands, in 2015.

Since 2018, she has been an Assistant Professor of microwave remote sensing with ITC, University of Twente, Enschede, the Netherlands. Her research interests include statistical hypothesis testing, time series modeling, and change detection, using satellite-borne remote sensing technology.

Jicang Wu received B.E. degree from the Department of Geomatics, Wuhan Technical University of Surveying and Mapping, Wuhan, China, in 1986, the M.S.E. degree from the Department of Surveying from Tongji University, Shanghai, China, in 1989, and the Ph.D. degree from the Department of Land Surveying and Geo-Informatics, The Hong Kong Polytechnic University, Hong Kong, in 1998.

He has been a Professor with the College of Surveying and Geo-Informatics, Tongji University. He is specialized in crustal deformation monitoring and inversion analysis.

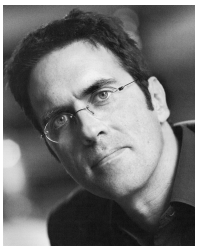

Ramon F. Hanssen (Senior Member, IEEE) received the M.Sc. degree in geodetic engineering and the Ph.D. degree *(cum laude)* from the Delft University of Technology, Delft, The Netherlands, in 1993 and 2001, respectively.

He was with the International Institute for Aerospace Survey and Earth Science (ITC), Stuttgart University, Stuttgart, Germany; the German Aerospace Center (DLR), Weßling, Germany; Stanford University, Stanford, CA, USA, as a Fulbright Fellow; and the Scripps Institution of Oceanography, University of California at San Diego, La Jolla, CA, USA, involved in microwave remote sensing, radar interferometry, signal processing, and geophysical application development. Since 2008, he has been an Antoni van Leeuwenhoek Professor of earth observation with the Delft University of Technology, where he has been leading the Research Group on mathematical geodesy and positioning since 2009. He has authored a textbook on radar interferometry.